https://doi.org/10.1007/s41230-024-3059-0

Effect of droplet characteristics on liquid-phase distribution in spray zone of internal mixing air-mist nozzle

Wei-li Wu[1, 2], Chang-gui Cheng[1, 2], *Yang Li[1, 2], Shi-fa Wei[1, 2], and De-li Chen[3]

1. The State Key Laboratory of Refractories and Metallurgy, Wuhan University of Science and Technology, Wuhan 430081, China

2. Hubei Provincial Key Laboratory for New Processes of Ironmaking and Steelmaking, Wuhan University of Science and Technology, Wuhan 430081, China

3. Technology Center, Fushun Special Steel Co., Ltd., Fushun 113001, Liaoning, China

Abstract: In continuous casting production, droplet characteristics are important parameters for evaluating the nozzle atomization quality, and have a significant impact on the secondary cooling effect and the slab quality. In order to study the behavior of atomized droplets after reaching the slab surface and to optimize the spray cooling effect, the influence of droplet diameter and droplet velocity on the migration behavior of droplets in the secondary cooling zone was analyzed by FLUENT software. Results show that the droplets in the spray zone and on the slab surface are mainly concentrated in the center, thus, the liquid volume fraction in the center is higher than that of either side. As the droplet diameter increases, the region of high liquid volume fraction on the slab surface becomes wider, and the liquid phase distribution in the slab width direction becomes uneven. Although increasing the droplet velocity at the nozzle exit has little effect on droplet diffusion in the spray zone, the distribution becomes more uneven due to more liquid reaches the slab surface per unit time. A prediction formula of the maximum water flow rate on the slab surface for specific droplet characteristics was proposed based on dimensionless analysis and validated by simulated data. A nozzle spacing of 210 mm was recommended under the working conditions in this study, which ensures effective coverage of the spray water over the slab surface and enhances the distribution uniformity of water flow rate in the transverse direction.

Keywords: continuous casting; secondary cooling zone; internal mixing air-mist nozzle; droplet characteristics; liquid phase distribution; water flow rate

CLC numbers: TP391.9 **Document code:** A **Article ID:** 1672-6421(2024)02-185-12

1 Introduction

The heat transfer behavior between the atomized droplets formed by the nozzles and the high temperature slab is the key factor affecting the cooling efficiency in the secondary cooling zone during continuous casting [1-3]. At present, the internal mixing air-mist nozzle is widely used in continuous slab casting process due to its advantages of low possibility of blockage, wide adjustment range of mass flow rate, uniform cooling, high cooling rate, and less residual water on the slab surface [4, 5]. The atomization principle of an internal mixing air-mist nozzle is that the cooling water flows to the nozzle core and is then ejected from the water orifice to form large water droplets, and then the large droplets are broken into smaller ones by the lateral shearing action of the high-speed air jet. The air and water droplets are completely mixed in the mixing chamber, while the droplets are accelerated and collide with each other under the entrainment action of the air jet. Finally, they are ejected at the nozzle exit, forming atomized air-water two-phase flow with high impact [6, 7]. The droplets ejected from the secondary cooling nozzle have a certain diameter and velocity, which directly affects the heat transfer behavior between the atomized droplets and the high temperature slab.

***Yang Li**

Ph. D, Associate Professor. Her research interests mainly focus on quality control of continuous casting strands and optimization of continuous casting process. She has presided over/participated in projects supported by the National Natural Science Foundation of China Youth Science Fund, Chinese Postdoctoral Science Fund, and National Natural Science Foundation of China, etc.

E-mail: liyang@wust.edu.cn

Received: 2023-05-15; Accepted: 2023-12-29

Many researchers have focused on the effect of process parameters and internal structure on the atomization performance of the internal mixing air-mist nozzle. Watanawanyoo et al. [8] and Lal et al. [9] found that the droplet diameter decreased with increasing the relative gas-liquid velocity and the mass flow rate ratio of water to air. The droplet diameter firstly increased and then decreased with increasing the gas-liquid flow intersection angle [10], and decreased with a larger spraying angle [11], a greater number of air holes [12], and a smaller diameter of nozzle hole [13]. Cheng et al. [14] pointed out that the optimal mixing chamber length can result in the smallest atomization droplet diameter of the internal mixing nozzle. Pougatch et al. [15] and Minchaca et al. [16] showed that the droplet velocity gradually increased with increasing gas-liquid ratio from a certain value. Hernández et al. [17] and Han et al. [18] believed that increasing both air pressure and water pressure (water flow rate) at the nozzle inlet would increase the droplet velocity, with the influence of air pressure being more significant. Saha et al. [19] showed that the droplet motion velocity increased with increasing the nozzle exit aperture when the inlet pressures of air and water phases were constant. From the above study, the process and structural parameters of the nozzle have an important influence on the diameter and velocity of the droplets ejected from the nozzle. The droplet characteristics are crucial for the heat transfer performance of the slab, which can ultimately affect the quality of slab [20].

The high heat transfer efficiency and cooling uniformity in the secondary cooling zone are important for the high-speed continuous casting process, which are related to the cooling water flow rate [21, 22], cooling water characteristics [23], slab surface temperature [24], and casting speed [25]. The water flow density distribution on the slab surface is an important parameter to evaluate the cooling effect and uniformity of slab in the secondary cooling zone [26]. Unreasonable distribution of water flow density on the slab surface is prone to slab defects such as center cracks, corner cracks, and segregation [27]. According to the results of the water flow rate distribution measurement of a fan-shaped air-assist nozzle with a spraying angle of 90° by Ji et al. [28], the water flow rate was distributed as a Gaussian distribution, in which the highest point of the water flow rate was at the centerline of the nozzle, and water flow rate gradually decreased from the center to the edges of the slab. Preuler et al. [29] showed that the water flow density on the slab surface increased with increasing the water flow rate of nozzle. When the water flow rate was constant, the sum of water flow density in the strand width direction did not change with increasing the air pressure, and the maximum water flow density increased slightly. Results of water flow density distribution under different inlet water flow rates showed that the water flow density was with central symmetry. As the water flow rate increased, the water flow density increased correspondingly, but the extent of increase was more pronounced in the center [30]. Ma et al. [31, 32] found that as the distance between the tip of the fan-shaped nozzle and the slab surface increased under a constant total water flow rate, the coverage of the secondary cooling water on the slab surface increased, and the water flow rate in the corners increased while that in the center decreased, thus the distribution of the secondary cooling water became more homogenous in the traverse direction. Similar conclusions were obtained by Zhang et al. [33] and Xia et al. [34]. These studies have implications for understanding the migration behavior of droplets after leaving the nozzle in the spray zone and the distribution uniformity of water flow density on the slab surface.

There are few studies on the effect of droplet characteristics on droplet migration in spray zone and liquid phase distribution on the slab surface. Yan et al. [35] suggested the droplet characteristics affected the spatial distribution of spray. They found that an increase in droplet velocity and droplet diameter led to a longer lateral distance and a larger coverage area due to the atomized droplet. However, the characteristic values of droplets in the above study are quite different from those in actual continuous casting secondary cooling zone, and the relationship between the droplet characteristics and quantity or distribution of water flow rate on the slab surface is not clear. In this study, a three-dimensional numerical model of the spray zone of the internal mixing air-mist nozzle was established by CFD software to investigate the influence of droplet diameter and droplet velocity on the migration behavior of droplets in the secondary cooling zone. In addition, the influence of nozzle arrangement on the secondary cooling effect was discussed, and the prediction formula of the maximum water flow rate on the slab surface under different droplet characteristics was also proposed. The results can provide a theoretical basis and reference for the optimization of secondary cooling system in continuous slab casting process, and are conducive to the further study how droplet characteristics impact the heat transfer behavior of the slab surface within the secondary cooling zone.

2 Mathematical model

2.1 Assumption

In view of the complexity of air-water two-phase atomization, the following assumptions were made in this study:

(1) Only the nozzle atomization process in cold state was considered, and the influence of heat transfer on atomization was not considered;

(2) The liquid phase was regarded as an incompressible fluid, and its density and viscosity were set to a constant;

(3) The lift force of gas phase and the virtual mass force between gas and liquid phases could be ignored;

(4) The atomized droplets were assumed to be spherical in the migration process, and their diameters were identical under the same working conditions;

(5) The influence of droplet number on liquid phase distribution was not considered.

2.2 Governing equations

The Eulerian two-phase flow model was used to simulate the gas-liquid two-phase flow in the spray zone of the nozzle. Liquid and gas phases interacted intensively in the air-mist nozzle, and two phases were interspersed with each other. In order to descript the air-water two-phase flow as interpenetrating continua, the concept of phase volume fraction was introduced, which was denoted as α_q, where the subscript q stands for the air (a) or water (w) phase. The volume fraction represented the space occupied by each phase, and each phase independently satisfied the conservation laws of mass and momentum. The sum of the volume fractions in all phases is 1, that is

$$\sum_{q=1}^{n} \alpha_q = 1 \tag{1}$$

The continuity and momentum equations for phase q are as follows:

$$\frac{\partial}{\partial t}\left(\alpha_q \rho_q\right) + \nabla\left(\alpha_q \rho_q \boldsymbol{v}_q\right) = 0 \tag{2}$$

$$\begin{aligned} &\frac{\partial}{\partial t}\left(\alpha_q \rho_q \boldsymbol{v}_q\right) + \nabla \cdot \left(\alpha_q \rho_q \boldsymbol{v}_q \boldsymbol{v}_q\right) \\ &= \nabla \cdot \boldsymbol{\tau}_q - \alpha_q \nabla P + \alpha_q \rho_q \boldsymbol{g} + \boldsymbol{F}_{\mathrm{d},q} \end{aligned} \tag{3}$$

where t is the time, s; ρ_q is the density, kg·m^{-3}; $\boldsymbol{v}_q$ is the velocity, m·s^{-1}; $\boldsymbol{\tau}_q$ is the stress-strain tensor, N·m^{-2}; P is the pressure, Pa; $\boldsymbol{g}$ is the gravitational acceleration, m·s^{-2}; and $\boldsymbol{F}_{\mathrm{d},q}$ is the drag force, N·m^{-3}. $\boldsymbol{\tau}_q$ and $\boldsymbol{F}_{\mathrm{d,w}}$ [36] are presented as follows:

$$\boldsymbol{\tau}_q = \alpha_q \eta_q (\nabla \boldsymbol{v}_q + \nabla \boldsymbol{v}_q^{\mathrm{T}}) + \alpha_q \left(\lambda_q - \frac{2}{3}\eta_q\right) \nabla \cdot \boldsymbol{v}_q \boldsymbol{I} \tag{4}$$

$$\boldsymbol{F}_{\mathrm{d,w}} = \frac{1}{8}\pi C_{\mathrm{D}} \rho_{\mathrm{a}} d^2 \left|\boldsymbol{v}_{\mathrm{a}} - \boldsymbol{v}_{\mathrm{w}}\right| \left(\boldsymbol{v}_{\mathrm{w}} - \boldsymbol{v}_{\mathrm{a}}\right) \tag{5}$$

where η_q and λ_q are the shear and bulk viscosities, respectively, Pa·s; $\boldsymbol{I}$ is the unit tensor; d is the droplet diameter, m; C_{D} is the drag coefficient and calculated as:

$$C_{\mathrm{D}} = \begin{cases} \dfrac{24\left(1 + 0.15 Re^{0.687}\right)}{Re} & Re \le 1000 \\ 0.44 & Re > 1000 \end{cases} \tag{6}$$

where Re is the relative Reynolds number, which is defined as:

$$Re = \frac{\rho_{\mathrm{a}} \left|\boldsymbol{v}_{\mathrm{a}} - \boldsymbol{v}_{\mathrm{w}}\right| d}{\mu_{\mathrm{a}}} \tag{7}$$

where μ_{a} is the molecular viscosity of air phase, Pa·s.

The mixture κ-ε turbulence model was adopted. The transport equations for the turbulence kinetic energy (κ) and its dissipation rate (ε) are as follows:

$$\begin{aligned} &\frac{\partial}{\partial t}\left(\rho_{\mathrm{m}} \kappa\right) + \nabla \cdot \left(\rho_{\mathrm{m}} \boldsymbol{v}_{\mathrm{m}} \kappa\right) \\ &= \nabla \cdot \left(\frac{\mu_{t,\mathrm{m}}}{\sigma_\kappa} \nabla \kappa\right) + G_{\kappa,\mathrm{m}} - \rho_{\mathrm{m}} \varepsilon \end{aligned} \tag{8}$$

$$\begin{aligned} &\frac{\partial}{\partial t}\left(\rho_{\mathrm{m}} \varepsilon\right) + \nabla \cdot \left(\rho_{\mathrm{m}} \boldsymbol{v}_{\mathrm{m}} \varepsilon\right) \\ &= \nabla \cdot \left(\frac{\mu_{t,\mathrm{m}}}{\sigma_\varepsilon} \nabla \varepsilon\right) + C_{1\varepsilon} \frac{\varepsilon}{\kappa} G_{\kappa,\mathrm{m}} - C_{2\varepsilon} \rho_{\mathrm{m}} \frac{\varepsilon^2}{\kappa} \end{aligned} \tag{9}$$

where $C_{1\varepsilon}$, $C_{2\varepsilon}$, σ_κ, and σ_ε are the constants, and their values are 1.44, 1.92, 1.0 and 1.3, respectively; the subscript m denotes the mixture of the two phases; ρ_{m}, $\boldsymbol{v}_{\mathrm{m}}$, $\mu_{t,\mathrm{m}}$, and $G_{\kappa,\mathrm{m}}$ are the density, velocity, viscosity, and production of turbulence kinetic energy for mixture, respectively, which are calculated as follows:

$$\rho_{\mathrm{m}} = \alpha_{\mathrm{a}} \rho_{\mathrm{a}} + \alpha_{\mathrm{w}} \rho_{\mathrm{w}} \tag{10}$$

$$\boldsymbol{v}_{\mathrm{m}} = \frac{\alpha_{\mathrm{a}} \rho_{\mathrm{a}} \boldsymbol{v}_{\mathrm{a}} + \alpha_{\mathrm{w}} \rho_{\mathrm{w}} \boldsymbol{v}_{\mathrm{w}}}{\alpha_{\mathrm{a}} \rho_{\mathrm{a}} + \alpha_{\mathrm{w}} \rho_{\mathrm{w}}} \tag{11}$$

$$\mu_{t,\mathrm{m}} = \rho_{\mathrm{m}} C_\mu \frac{\kappa^2}{\varepsilon} \tag{12}$$

$$G_{\kappa,\mathrm{m}} = \frac{\mu_{t,\mathrm{m}} \left(\nabla \boldsymbol{v}_{\mathrm{m}} + \left(\nabla \boldsymbol{v}_{\mathrm{m}}\right)^T\right)}{\nabla \boldsymbol{v}_{\mathrm{m}}} \tag{13}$$

where C_μ is the empirical constant, with a value of 0.09; α_{a} (α_{w}), ρ_{a} (ρ_{w}), and $\boldsymbol{v}_{\mathrm{a}}$ ($\boldsymbol{v}_{\mathrm{w}}$) are the volume fraction, density, and velocity of air (water) phase, respectively.

2.3 Boundary conditions and numerical method

Figure 1 shows the structure of the internal mixing air-mist nozzle used in this study, where the section plane and three-dimensional model of the nozzle are shown in Figs. 1(a) and (b), respectively. The geometric parameters of the internal mixing nozzle are shown in Table 1. Based on our previous research [37, 38], the hemispherical outlet of the mixing chamber in Fig. 1 was considered as the inlet of the nozzle spray zone model. The overall three-dimensional geometry of the spray zone and the local mesh structure near the inlet are shown in Fig. 2. In the simulation calculation of air-mist nozzle cooling for continuously cast slab, the spray field was divided by hexahedral structure mesh due to its regularity. The meshes at the nozzle exit and the slab surface were refined with a minimum diameter of 0.2 mm.

In the actual continuous casting process, the spray distance between the secondary cooling nozzle tip and the slab surface is about 100–200 mm [39]. In this study, the spray height was set at 140 mm, and the spray water coverage was about 600 mm across the width of the slab transverse direction. The optimal droplet diameter range of air-mist nozzle is about 0.02–0.05 mm [40]. According to our previous simulation results in the internal flow field of the internal mixing nozzle, the average velocity of liquid phase (droplets) at the hemispherical outlet of the mixing chamber is in the range of 30–60 m·s^{-1} [37]. The droplet parameters in the numerical simulation of this study are shown in Table 2.

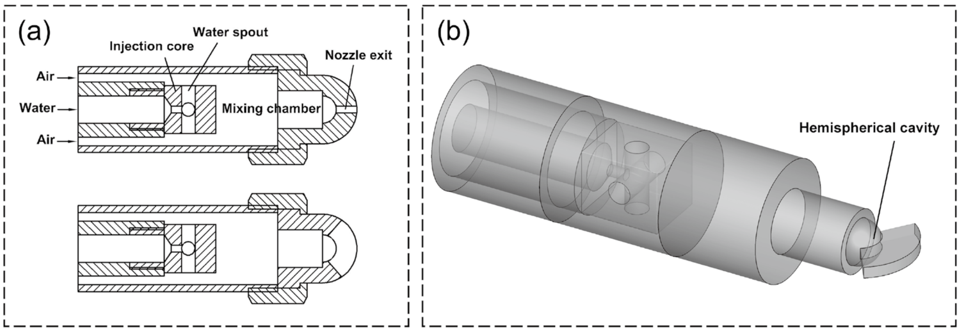

Fig. 1: Structure diagram of traditional internal mixing nozzle: (a) section plane views; (b) three-dimensional model

In Fig. 2, a velocity boundary condition was used for the inlet, and the direction of velocity was normal to the boundary flowing into the computational domain direction. The spray field was set as the boundary condition of the pressure outlet. The outlet pressure was set to 1 atm, and the liquid volume fraction at the outlet was 0, which meant that there was only air phase at the beginning of computational process. All walls were defined as non-slip conditions, and standard wall functions were used to solve them. The SIMPLE algorithm was chosen for the coupling of pressure and velocity terms, and the PRESTO scheme was used for pressure discretization. The second-order upwind difference scheme was employed for all variables including momentum, volume fraction, turbulent kinetic energy, and turbulent dissipation rate. The time step was fixed at 0.001 s. The residual of the continuity equation was stable between 10^{-3} and 10^{-4}, and all the values of remaining arguments were below 10^{-4}, indicating that the numerical simulation results had reached convergence for each operating condition.

Table 1: Geometric parameters of internal mixing nozzle

Parameters	Values
Inner diameter of air inlet pipe (mm)	21
Outer diameter of air inlet pipe (mm)	25
Inner diameter of water inlet pipe (mm)	8
Outer diameter of water inlet pipe (mm)	16
Side length of injection core (mm)	14
Water spout diameter (mm)	4
Mixing chamber length (mm)	31
Hemispherical outlet diameter of mixing chamber (mm)	8
Nozzle outlet width (mm)	2
Nozzle outlet angle (°)	110

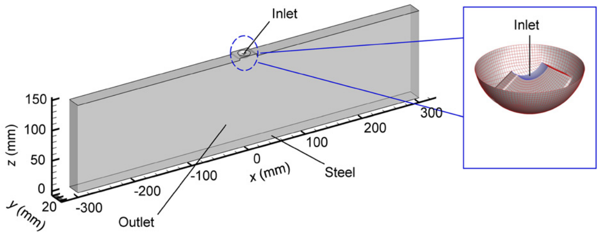

Fig. 2: Schematic of overall geometry and local mesh models of spray zone

Table 2: Droplet parameters used in the numerical simulation

Parameters	Values
Density (kg·m^{-3})	998.2
Viscosity (Pa·s)	0.001003
Droplet diameter (mm)	0.02, 0.03, 0.04, 0.05
Droplet velocity (m·s^{-1})	30, 40, 50, 60

2.4 Mesh independence study

In order to analyze the correlation between the calculation results and the mesh diameter, simulations were carried out with a droplet diameter of 0.03 mm and droplet velocity of 50 m·s^{-1}, for the cases of 2.54 million, 3.1 million, 3.62 million and 4.43 million meshes. The water mass flow rate distribution on the slab surface under different number of meshes was compared and the results are shown in Fig. 3.

From Fig. 3, it can be observed that the water flow rate distribution on the slab surface is almost consistent, which means the number of meshes has little effect on the simulation results. To achieve a balance between computational workload and calculation accuracy, a mesh of 3.1 million was used in this study.

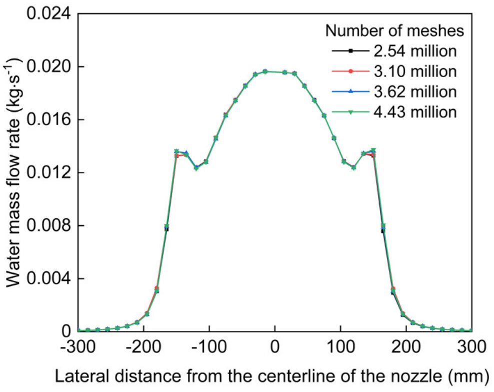

Fig. 3: Water mass flow rate distribution on the slab surface under different number of meshes

3 Simulation results

3.1 Model verification

To further verify the reliability of the mathematical model, an experimental platform for measuring the water flow density of the secondary cooling nozzle was established to observe the migration behavior of atomized droplets in the spray zone and the water flow rate distribution across the slab surface. The nozzles used in this experiment have the same structure as the simulation, and their parameters are shown in Table 3. The comparison of experimental data with simulation results is shown in Fig. 4.

Figures 4(a) and (b) show the spraying angle and the water flow rate distribution on the slab surface obtained by simulation and experiment, respectively. The angle between the two tangents from the center point of nozzle exit to the outer boundary of the cone (fan) shaped flow field is called the spraying angle [41]. In Fig. 4(a), the spraying angle obtained from the numerical model of the spray zone is 127.8°, and the experimental value is 128.1°, with an error of 0.23%. Figure 4(b) indicates that the overall trends of both the statistical data in numerical simulation and the experimental measurement data are similar. The water flow rate is the largest near the center of slab surface, and it gradually decreases from the center to both sides. Additionally, the atomization range is roughly the same in both cases. Compared with the simulation curve, there is a gap in the center of the experimental curve, that is, the water flow rate at the center of slab surface is slightly lower than that in the surrounding region. This may be caused by measurement errors in the experiment. However, considering that the simulation outcomes for both the spraying angle and water flow rate distribution closely match the actual measured values, it can be concluded that the mathematical model is reliable.

Table 3: Experimental and simulation parameters of spray cooling in the secondary cooling zone

Parameters	Experiment	Simulation
Air supply pressure (MPa)	0.3	–
Water supply pressure (MPa)	0.5	–
Air flow rate ($m^3 \cdot h^{-1}$)	3.1	–
Water flow rate ($L \cdot h^{-1}$)	325	–
Spray height (mm)	140	140
Droplet diameter (mm)	–	0.03
Droplet velocity ($m \cdot s^{-1}$)	–	30

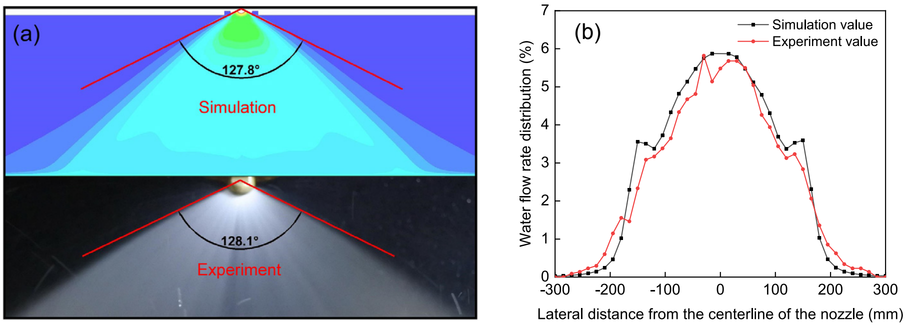

Fig. 4: Comparison between measurement and simulation results

3.2 Effect of droplet diameter on liquid phase distribution

Figure 5 shows the liquid phase distribution of the center cross-section along the Y axis (hereinafter referred to as the center section) in the spray zone under different droplet diameters when the droplet velocity is 50 $m \cdot s^{-1}$. The water droplets are spout out in a fan shape from the nozzle exit. The volume fraction of droplets is the highest at the nozzle exit, and it gradually decreases during the diffusion process. The atomized droplets of spray zone are mainly concentrated in the center, and thus the liquid volume fraction is higher in the center than that of either side. By comparing Figs. 5(a), (b), (c) and (d), it can be found that the droplets occupy the greatest migration range with a droplet diameter of 0.02 mm. And the diffusion range tends to decrease as the droplet diameter increases.

In order to quantitatively analyze the effect of droplet diameter on its migration behavior in the spray zone, the measured spraying angle under different droplet diameters is shown in Fig. 6, which is obtained by improving the brightness of Fig. 5. Figure 6 shows that the spraying angle is the largest when the droplet diameter is 0.02 mm, which corresponds to the largest droplet migration range in the spray zone. This is related to the droplet kinetic energy and the air drag force [42]. The kinetic energy ($E_k = 1/2 m \boldsymbol{v}_w^2$) of a droplet is determined by its mass (m) and the square of droplet velocity ($\boldsymbol{v}_w$), where m is proportional to the cube of droplet diameter (d). Since the air velocity is much lower than the droplet velocity in the spray zone, there is a positive correlation between the air drag force and droplet diameter according to Eq. (5) under the premise of neglecting the air velocity. It can be inferred that both the droplet kinetic energy and the air drag force increase with increasing the droplet diameter at a certain droplet velocity. The kinetic energy of the droplet helps it to spread, while the air drag force prevents the droplet from spreading. Consequently, the air drag force has a relatively greater effect on the droplet migration, and the diffusion range of droplets gradually decreases with increasing the droplet diameter.

Figure 7 shows the liquid phase distribution on the slab surface under different atomized droplet diameters. The liquid volume fraction is the largest at the center of slab surface, and gradually decreases from the center to both sides. A larger droplet diameter enlarges the region of high liquid volume fraction on the slab surface. The computational domain was divided into 40 parts along the width direction to quantify the water flow rate distribution on the slab surface under different droplet diameters, as shown in Fig. 8. When the atomized droplet diameter increases from 0.02 mm to 0.05 mm, the maximum water mass flow rate on the slab surface increases from 0.014 kg·s^{-1} to 0.034 kg·s^{-1}. This indicates that as the droplet diameter increases, more cooling water reaches the slab surface per unit time at a constant droplet velocity, which is conducive to enhancing the cooling strength of the slab in the secondary cooling zone.

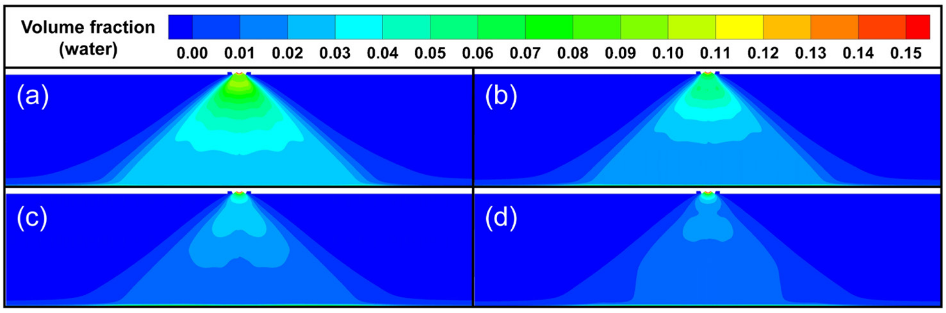

Fig. 5: Liquid-phase distribution at the center section under different droplet diameters: (a) 0.02 mm; (b) 0.03 mm; (c) 0.04 mm; (d) 0.05 mm

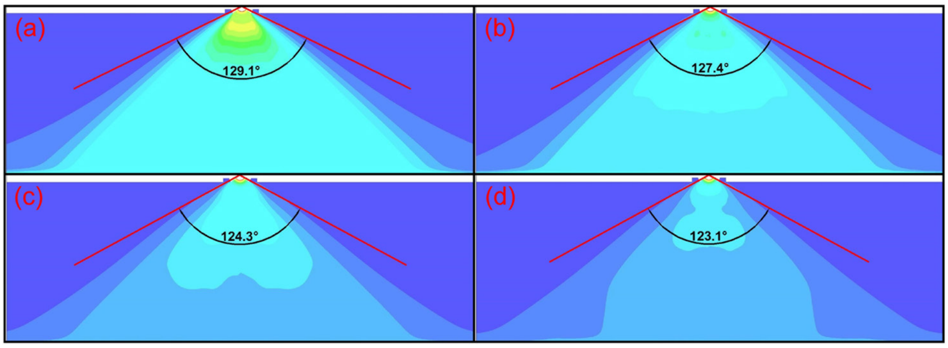

Fig. 6: Spraying angle under different droplet diameters: (a) 0.02 mm; (b) 0.03 mm; (c) 0.04 mm; (d) 0.05 mm

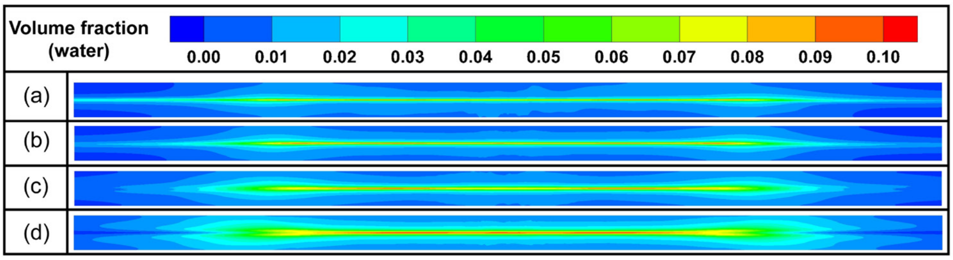

Fig. 7: Liquid-phase distribution on the slab surface under different droplet diameters: (a) 0.02 mm; (b) 0.03 mm; (c) 0.04 mm; (d) 0.05 mm

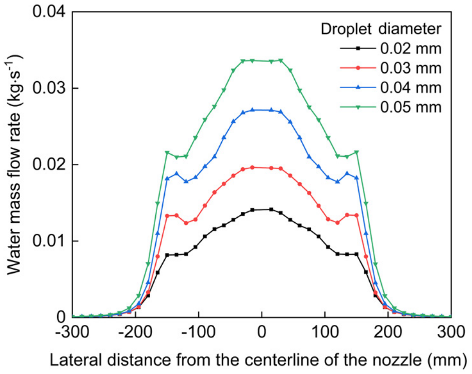

Fig. 8: Water mass flow rate distribution on the slab surface under different droplet diameters

Based on the discussion above, it can be concluded that a smaller droplet diameter decreases the water content within a single droplet, while the atomization range is larger. In this case, some of droplets will leave the simulation region and not fall on the slab surface. On the contrary, when the droplet diameter is larger, more droplets will fall on the slab surface due to the reduction of the atomization range. Based on the above two points, a larger droplet diameter increases the water flow density on the slab surface. However, the liquid phase distribution on the slab surface becomes more uneven due to the increment of the atomized droplet diameter, which will reduce the cooling uniformity of slab and may ultimately lead to the quality defects of slab.

3.3 Effect of droplet velocity on liquid phase distribution

When the droplet diameter is 0.03 mm, the liquid phase distribution at the center section of the spray zone under different droplet velocities is shown in Fig. 9. The spraying angle of the nozzle is shown in Fig. 10, and the liquid phase distribution on the slab surface is shown in Fig. 11.

As shown in Figs. 9 and 10, the migration range of droplets in the spray zone is basically the same with increasing droplet velocity at a given droplet diameter. The spraying angles are 127.8°, 127.2°, 127.4° and 126.9°, corresponding to droplet velocities of 30 $m\cdot s^{-1}$, 40 $m\cdot s^{-1}$, 50 $m\cdot s^{-1}$ and 60 $m\cdot s^{-1}$, respectively. The difference in nozzle spraying angle under different droplet velocities is not significant, which demonstrates that the droplet velocity has little effect on the droplet diffusion in the spray zone. This is related to the dual action of droplet kinetic energy and air drag force as mentioned in Section 3.2. When other factors remain unchanged, a larger droplet velocity leads to greater kinetic energy possessed by the droplet, but this also leads to a more obvious obstruction effect of air on the droplet. Therefore, it can be inferred that the diffusion range of droplets is basically the same under the action of droplet kinetic energy and air drag force for four droplet velocities in this study. Figure 11 shows that the region of high liquid volume fraction on the slab surface increases slightly with increasing atomized droplet velocity, indicating that more liquid phases reach the slab surface per unit time.

Figure 12 shows the distribution of water mass flow rate along the width direction of the slab surface under different droplet velocities. It can be seen that the liquid phase is mainly concentrated in the region [–250 mm, 250 mm] on the slab surface. The variation of mass flow rate presents a symmetrical mountain peak curve. For all working conditions, the water flow rate reaches its maximum value in the main flow region and decreases towards both sides. It is worth noting that all curves show two plateau periods in the intervals of [–150 mm, –120 mm] and [120 mm, 150 mm], where the water flow rate is basically unchanged or shows a slightly increasing trend. The main reason is that this region is the transition region where the droplets are subject to a combination of kinetic energy and air drag force [33]. In the region [–120 mm, 120 mm], the droplet kinetic energy is relatively large, and a large number of droplets

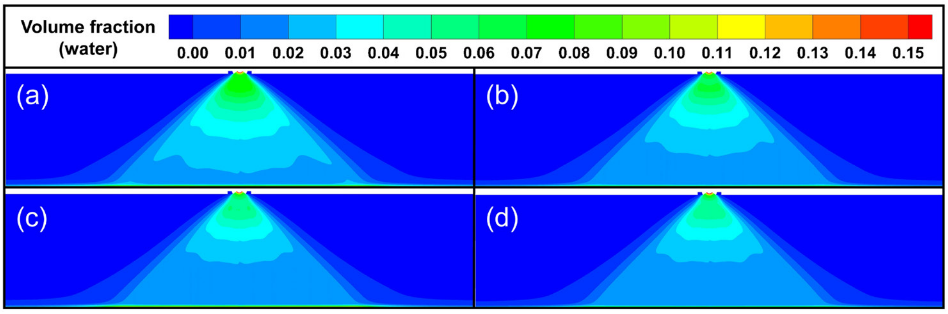

Fig. 9: Liquid-phase distribution at the center section under different droplet velocities: (a) 30 $m\cdot s^{-1}$; (b) 40 $m\cdot s^{-1}$; (c) 50 $m\cdot s^{-1}$; (d) 60 $m\cdot s^{-1}$

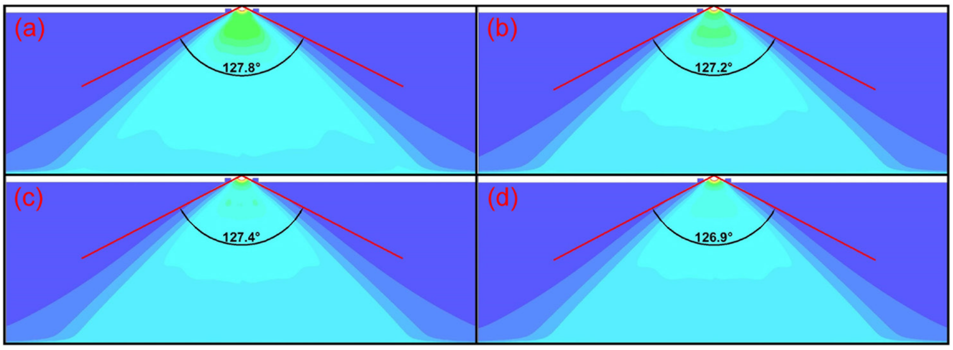

Fig. 10: Spraying angle under different droplet velocities: (a) 30 $m\cdot s^{-1}$; (b) 40 $m\cdot s^{-1}$; (c) 50 $m\cdot s^{-1}$; (d) 60 $m\cdot s^{-1}$

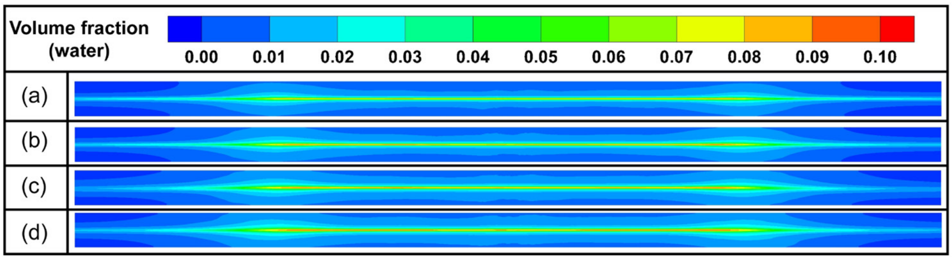

Fig. 11: Liquid-phase distribution on the slab surface under different droplet velocities: (a) 30 $m\cdot s^{-1}$; (b) 40 $m\cdot s^{-1}$; (c) 50 $m\cdot s^{-1}$; (d) 60 $m\cdot s^{-1}$

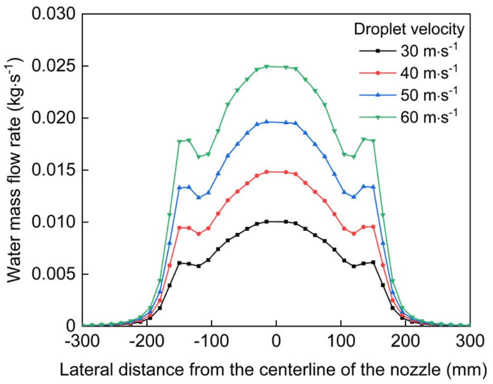

Fig. 12: Water mass flow rate distribution on the slab surface under different droplet velocities

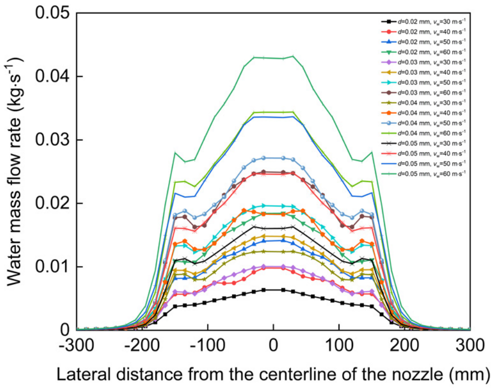

Fig. 13: Water mass flow rate distribution on the slab surface under different droplet characteristics

overcome the air drag force to reach the slab surface. As the droplets continue to spread, air drag force begins to dominate and the droplet kinetic energy decreases sharply in the regions [−250 mm, −150 mm] and [150 mm, 250 mm], resulting in a significant decrease in the water mass flow rate on the slab surface. In addition, the width of liquid phase distribution has little change with increasing the droplet velocity. Figure 12 shows the same trend as the Figs. 9, 10, and 11. However, the liquid phase reaching the slab surface gradually increases per unit time with increasing the droplet velocities, among which the center zone increases significantly. From the center of the slab to its edges, the degree of increase in water flow rate gradually descends along the width direction. This also increases the difference of water flow rate between the center and edges of the slab, and thus the liquid phase distribution on the surface becomes more uneven, which may eventually reduce the cooling uniformity of the slab.

4 Discussion and analysis

4.1 Prediction of maximum water flow rate on slab surface

Figure 13 shows the distribution curve of water mass flow rate in the width direction of the slab surface under different droplet diameters and droplet velocities. When both the droplet diameter and droplet velocity increase, the water flow rate on the slab surface tends to increase. When the droplet diameter increases from 0.02 mm (with a droplet velocity of 50 m·s^{-1}) to 0.03 mm (with a droplet velocity of 30 m·s^{-1}), the maximum water flow rate on the slab surface decreases from 0.014 kg·s^{-1} to 0.010 kg·s^{-1}, which is contrary to the pattern observed in Fig. 8 for the same droplet velocity. Similarly, the maximum water flow rate decreases from 0.018 kg·s^{-1} to 0.014 kg·s^{-1} when droplet velocity increases from 40 m·s^{-1} (with a droplet diameter of 0.04 mm) to 50 m·s^{-1} (with a droplet diameter of 0.02 mm), which is contrary to the pattern observed in Fig. 12 for the same droplet diameter. These indicate that the maximum water flow rate on the slab surface is not determined solely by the droplet diameter or the droplet velocity, but by both together.

In order to characterize the influence of droplet characteristics on the water flow rate across the slab surface, a relationship expression between the maximum water flow rate on the slab surface and the droplet diameter or droplet velocity was established on the basis of dimensionless analysis, as follows:

$$W = k_1 D^{k_2} V^{k_3} \tag{14}$$

where, W, D and V are dimensionless maximum water flow rate, dimensionless droplet diameter, and dimensionless droplet velocity, respectively; k_1, k_2 and k_3 are dimensionless constants. The expressions of W, D, and V are as follows:

$$W = \frac{w}{\rho \boldsymbol{v}_{\max} s} \tag{15}$$

$$D = \frac{d}{d_{\max}} \tag{16}$$

$$V = \frac{\boldsymbol{v}_{\mathrm{w}}}{\boldsymbol{v}_{\max}} \tag{17}$$

where w is the maximum water flow rate on the slab surface, kg·s^{-1}; $d_{\max}$ is the maximum droplet diameter, which is a constant, and its value is 5×10^{-5} m; $\boldsymbol{v}_{\max}$ is the maximum droplet velocity, which is constant, and its value is 60 m·s^{-1}; ρ is the density of water, taken as 10^3 kg·m^{-3}; s is the inlet area of the computational domain, with a value of 2.02×10^{-5} m^2.

Combining Eqs. (15), (16) and (17), the correlation is given as following by performing logarithmic transformation and multiple non-linear regression analysis on Eq. (14):

$$w = 1.244528 d^{0.95309} \boldsymbol{v}_{\mathrm{w}}^{1.43249} \rho \boldsymbol{v}_{\max} s, \quad R^2 = 0.99519 \tag{18}$$

where R^2 is the coefficient of determination, a goodness of fit measure [43].

From Eq. (18), it can be seen that the maximum water flow rate is positively correlated with the droplet diameter and the droplet velocity. As the indices of the variables d and $\boldsymbol{v}_{\mathrm{w}}$ in Eq. (18) are 0.95309 and 1.43249, respectively, the effect of droplet velocity on the maximum water flow rate is more significant compared to the droplet diameter. From Fig. 8, when the droplet diameter increases from 0.02 mm to 0.03 mm, from 0.03 mm to 0.04 mm, and from 0.04 mm to 0.05 mm, the maximum water flow rate on the slab surface increases by 32.1%, 27.2%, and 29.0%, respectively. However, in Fig. 12, the percentage increases are 47.4%, 38.3%, and 32.9% when the droplet velocity increases from 30 m·s^{-1} to 40 m·s^{-1}, from

40 m·s^{-1} to 50 m·s^{-1}, and from 50 m·s^{-1} to 60 m·s^{-1}, respectively. It can be seen that the maximum water flow rate on the slab surface changes more significantly with the droplet velocity. Therefore, the regular patterns revealed in Figs. 8 and 12 are consistent with that of Eq. (18). This also indicates that the fitting formula is relatively accurate.

Figure 14 shows a comparison between the simulated maximum water flow rate and the maximum water flow rate fitted by Eq. (18) under different droplet diameters and velocities. The simulated and calculated values of the maximum water mass flow rate on the slab surface under different droplet characteristics are basically the same, proving the high accuracy of fitting equation. The results of maximum water flow rate for larger droplet diameters and higher droplet velocities are also predicted in Fig. 14. The results indicate that the values of maximum water flow rate show a continuous increasing trend without an inflection point. This indicates that the formula is suitable for cases where there are the changes in droplet velocity or diameter caused by high-speed continuous casting or modifications of nozzle structure (such as addition of the accelerating ring and changing of length or width in mixing chamber, etc.).

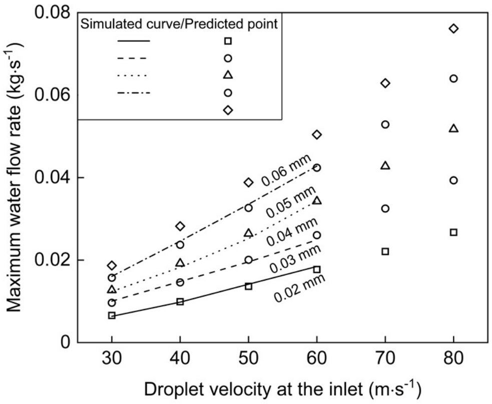

Fig. 14: Comparison between simulated and regression estimated maximum water flow rate under different droplet characteristics

In addition, the maximum water flow rates on the slab surface are 0.0249 kg·s^{-1}, 0.0252 kg·s^{-1} and 0.0246 kg·s^{-1} for three combinations of d=0.03 mm and v_w=60 m·s^{-1}, d=0.04 mm and v_w=50 m·s^{-1}, as well as d=0.05 mm and v_w=40 m·s^{-1}, respectively. There is no significant difference in the values of the maximum water flow rate for the above three cases. This means that similar maximum water flow rates can be obtained by reasonably adjusting the droplet diameters and velocities to achieve the required cooling intensity during continuous casting. Therefore, Eq. (18) can be used to predict the maximum water flow rate on the slab surface for a given droplet diameter and velocity, which is useful for controlling the secondary cooling intensity.

4.2 Effect of nozzle arrangement on secondary cooling effect

Due to the limited spraying range of a single nozzle, it cannot cover the entire width direction of continuously cast slab, and the difference in water flow density between the center of slab surface and its two sides is large. It will cause uneven cooling in the slab width direction, which is not conducive to improving the slab quality. Therefore, the combination of multiple nozzles is adopted to make water flow rate distribution more uniform along the width direction in actual production [44-46]. The principle of determining the spacing distance between adjacent nozzles is to ensure that the water flow rate is uniformly distributed along the slab width direction, which avoids the impact of water peak caused by nozzle superposition on the slab quality [47]. The empirical value of the optimal spacing distance between adjacent nozzles is calculated by Eq. (19) [48]:

$$l = 1.05 \cdot H \cdot \tan(\alpha / 2) \tag{19}$$

where l is the spacing between adjacent nozzles, mm; H is the spray height of the nozzle, mm; α is the spraying angle of the nozzle, °. In this study, the calculated optimal spacing is 210 mm as the spray height is 140 mm, and the spraying angle is 110°.

In order to further analyze the influence of nozzle arrangement on the secondary cooling effect, a numerical study of the water flow rate distribution on the slab surface under different spacings between adjacent nozzles was conducted. It is worth noting that this simulation was performed in the double-nozzle mode, rather than a simple superposition of the single-nozzle water flow rate in Fig. 13. The water flow rate distribution curves on the slab surface at a droplet diameter of 0.03 mm and droplet velocity of 40 m·s^{-1}, as well as at a droplet diameter of 0.04 mm and droplet velocity of 50 m·s^{-1} with spacings (l) of 180 mm, 210 mm, and 240 mm, respectively, are shown in Fig. 15. The origin of the abscissa axis in Figs. 15 and 16 is the axial centerline position of the first nozzle. The region between line segments A and B (referred to as Region AB) in Figs. 15(a) and (b) is the overlapping region of adjacent nozzles when l=180 mm, and Region AC and Region AD are overlapping regions at l=210 mm and l=240 mm, respectively.

Figure 15 shows that the superposition effect of double nozzles has an obvious downward trend with increasing the spacing, and the spray width of double nozzles becomes larger with increasing the spacing. There is a significant peak in the overlapping region at l=180 mm, indicating that the cooling intensity in this region is greater than in other regions. The peak value in the overlapping region is small at l=240 mm, but there is obvious peak to valley, indicating that the cooling effect is uneven. Compared with the above two spacings, the several peak values of water flow rate in the overlapping region show no obvious difference at l=210 mm, and the overall water flow density distribution is more uniform, indicating that the cooling effect is better than others. According to the calculation results of Eq. (19) and the water flow rate distribution results of different spacings in Fig. 15, it can be determined that the optimal spacing of the double-nozzle arrangement is 210 mm, which is in better line with the actual industrial situation [49].

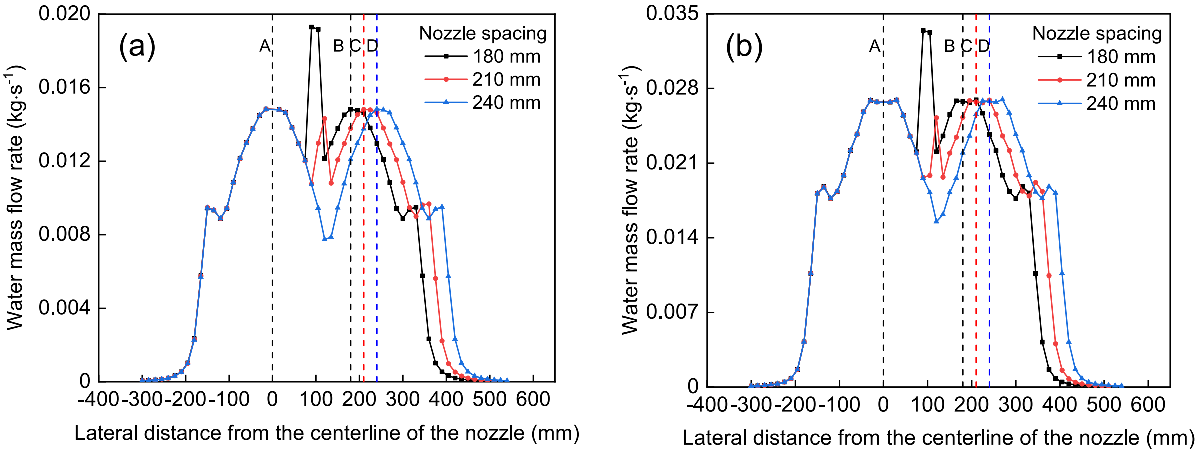

Fig. 15: Water mass flow rate distribution on the slab surface under different spacings and droplet characteristics: (a) droplet diameter of 0.03 mm, and droplet velocity of 40 m·s^{-1}; (b) droplet diameter of 0.04 mm, and droplet velocity of 50 m·s^{-1}

Figure 16 shows the water flow rate distribution on the slab surface after the superposition of adjacent nozzles under different droplet characteristics at a spacing of 210 mm. The coverage of spray water on the slab surface for this nozzle arrangement is 810 mm. In Fig. 16, the water flow density distribution is relatively uniform and the water flow rate is large in the overlapping Region A of adjacent nozzles, indicating that cooling effect of the slab is better. In Region B, which has the same range as the main atomization region of a single nozzle, the difference between the maximum and minimum water flow rates is 0.020 kg·s^{-1} at d=of 0.05 mm and v_w=60 m·s^{-1}, and the difference is 0.0038 kg·s^{-1} at d=0.02 mm and v_w=30 m·s^{-1}. However, for the same atomization range of single nozzle, the difference between the maximum and minimum water flow rates is 0.043 kg·s^{-1} at d=0.05 mm and v_w=60 m·s^{-1}, and the difference is 0.0063 kg·s^{-1} at d=0.02 mm and v_w=30 m·s^{-1}. As a result, the cooling uniformity is substantially improved by setting the nozzle arrangement reasonably within the main coverage region of 500 mm.

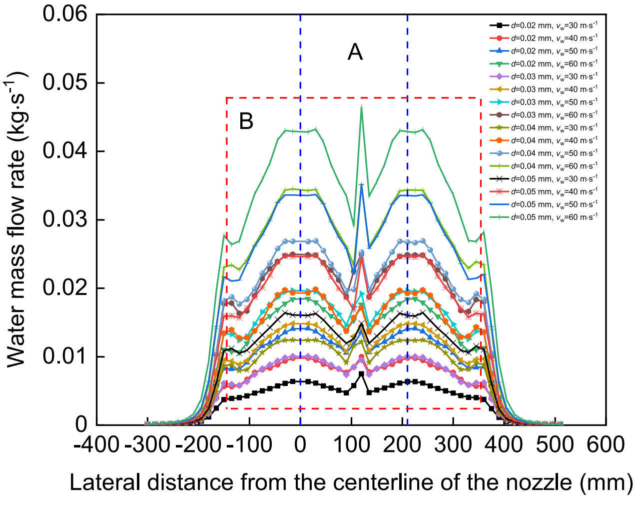

Fig. 16: Water mass flow rate distribution on the slab surface under different droplet characteristics at a spacing of 210 mm

Therefore, a reasonable nozzle arrangement (spacing) not only meets the coverage requirements for cooling water on the slab cross-section but also enhances the overlapping effectiveness of spray water. The cooling intensity of the overlapping region between adjacent nozzles is strengthened, and the water flow density distribution in a certain region from the center of slab surface to both sides in the transverse direction is more uniform. In the secondary cooling system of high-speed slab casting, multiple nozzles should be reasonably set in each row according to the maximum water flow rate and spray range of a single nozzle. It ensures not only the high cooling intensity but also the uniform cooling in entire slab transverse direction, which is conducive to the improvement of the slab quality.

5 Conclusions

(1) In the internal mixing air-mist nozzle, air and water are completely mixed in the nozzle and then ejected from the exit in a fan shape. The volume fraction of atomized droplets is the highest at the nozzle exit, and it gradually decreases during the diffusion process. In the spray zone, the droplets are mainly concentrated in the center, so the liquid volume fraction in the center is higher than that of either side. After the atomized droplets reach the slab surface, the liquid volume fraction is the largest in the center, and that gradually decreases from the center to both sides. The variation of mass flow rate shows a symmetrical peak curve under all working conditions, and the maximum water flow rate is located near the center of slab surface.

(2) When the droplet velocity remains constant, the region of high liquid volume fraction on the slab surface becomes wider with increasing the droplet diameter, but the liquid phase distribution becomes uneven in the slab width direction. In this case, both spraying angle of the nozzle and droplet diffusion range are the largest at a droplet diameter of 0.02 mm, and they are basically unchanged with the droplet velocity for a given droplet diameter. However, as the droplet velocity

increases, the water flow rate distribution on the slab surface becomes more uneven.

(3) The calculation formula of the maximum mass flow rate of secondary cooling water ejected from a single internal mixing air-mist nozzle on the slab surface is proposed. The correlation can be used to predict the maximum water flow rate on the slab surface at a given droplet diameter and droplet velocity, which can provide a theoretical basis for the optimization of the secondary cooling system.

(4) The secondary cooling water can cover the entire slab due to a reasonable nozzle arrangement, which ensures high cooling intensity in the lateral direction and effectively improves the cooling uniformity. Ultimately, it is conducive to minimizing slab defects and improving slab quality. A reasonable spacing of 210 mm between adjacent nozzles was determined under the working conditions in this study.

Acknowledgments

This work was funded by the National Natural Science Foundation of China (Nos. 51974213 and 52174324).

Conflict of interest

Authors declare that they have no conflict of interest.

References

[1] Zhang F J, Yang S F, Li J S, et al. Formation mechanism and control of transverse corner cracks in fine blanking steel. J. Mater. Res. Technol., 2022, 18: 1137–1146. https://doi.org/10.1016/j.jmrt.2022.03.042

[2] Yao C, Wang M, Zhang M Y, et al. Effects of mold electromagnetic stirring on heat transfer, species transfer and solidification characteristics of continuous casting round billet. J. Mater. Res. Technol., 2022, 19: 1766–1776. https://doi.org/10.1016/j.jmrt.2022.05.167

[3] Caron E, Wells M A. Film boiling and water film ejection in the secondary cooling zone of the direct-chill casting process. Metall. Mater. Trans. B, 2012, 43(1): 155–162. https://doi.org/10.1007/s11663-011-9579-1

[4] El-Bealy M O. Air-water mist and homogeneity degree of spray cooling zones for improving quality in continuous casting of steel. Steel Res. Int., 2011, 82(10): 1187–1206. https://doi.org/10.1002/srin.201000301

[5] Mlkvik M, Stahle P, Schuchmann H, et al. Twin-fluid atomization of viscous liquids: The effect of atomizer construction on breakup process, spray stability and droplet size. Int. J. Multiph. Flow, 2016, 77: 19–31. https://doi.org/10.1016/j.ijmultiphaseflow.2015.06.010

[6] Sovani S D, Sojka P E, Lefebvre A H. Effervescent atomization. Prog. Energy Combust. Sci., 2001, 27(4): 483–521. https://doi.org/10.1016/S0360-1285(00)00029-0

[7] Wu H, Zhang F J, Zhang Z Y. Droplet breakup and coalescence of an internal-mixing twin-fluid spray. Phys. Fluids, 2021, 33(1): 013317. https://doi.org/10.1063/5.0030777

[8] Watanawanyoo P, Mochida H, Furukawa T, et al. Experimental study on the spray characteristics of an air assisted atomizer with internal mixing chamber. Eur. J. Sci. Res., 2012, 84(4): 507–521. https://www.researchgate.net/publication/236214837

[9] Lal S, Kushari A, Gupta M, et al. Experimental study of an air assisted mist generator. Exp. Therm. Fluid Sci., 2010, 34(8): 1029–1035. https://doi.org/10.1016/j.expthermflusci.2010.03.006

[10] Avulapati M M, Venkata R R. Experimental studies on air-assisted impinging jet atomization. Int. J. Multiph. Flow, 2013, 57: 88–101. https://doi.org/10.1016/j.ijmultiphaseflow.2013.07.007

[11] Jedelsk J, Jícha M. Spray characteristics and liquid distribution of multi-hole effervescent atomizers for industrial burners. Appl. Therm. Eng., 2015, 96: 286–296. https://doi.org/10.1016/j.applthermaleng.2015.11.079

[12] Kushari A. Effect of injector geometry on the performance of an internally mixed liquid atomizer. Fuel. Process. Technol., 2010, 91(11): 1650–1654. https://doi.org/10.1016/j.fuproc.2010.06.014

[13] Sun H J, Luo Y K, Ding H B, et al. Experimental investigation on atomization properties of impaction-pin nozzle using imaging method analysis. Exp. Therm. Fluid Sci., 2021, 122: 110322. https://doi.org/10.1016/j.expthermflusci.2020.110322

[14] Cheng G, Fu C, Xu B B, et al. Internal mixing air-assisted spray nozzle for large droplets: Experimental measurements and numerical simulations. J. Aerosol. Sci., 2022, 65: 106035. https://doi.org/10.1016/j.jaerosci.2022.106035

[15] Pougatch K, Salcudean M, Chan E, et al. A two-fluid model of gas-assisted atomization including flow through the nozzle, phase inversion, and spray dispersion. Int. J. Multiph. Flow, 2009, 35(7): 661–675. https://doi.org/10.1016/j.ijmultiphaseflow.2009.03.001

[16] Minchaca J I, Castillejos A H, Acosta F A. Size and velocity characteristics of droplets generated by thin steel slab continuous casting secondary cooling air-mist nozzles. Metall. Mater. Trans. B, 2011, 42(3): 500–515. https://doi.org/10.1007/s11663-011-9501-x

[17] Hernández C A, Minchaca J I, Castillejos A H, et al. Measurement of heat flux in dense air-mist cooling: Part II – The influence of mist characteristics on steady-state heat transfer. Exp. Therm. Fluid Sci., 2013, 44: 161–173. https://doi.org/10.1016/j.expthermflusci.2012.06.007

[18] Han H, Wang P F, Li Y J, et al. Effect of water supply pressure on atomization characteristics and dust-reduction efficiency of internal mixing air atomizing nozzle. Adv. Powder Technol., 2020, 31(1): 252–268. https://doi.org/10.1016/j.apt.2019.10.017

[19] Saha A, Lee J D, Basu S, et al. Breakup and coalescence characteristics of a hollow cone swirling spray. Phys. Fluids, 2012, 24(12): 621–633. https://doi.org/10.1063/1.4773065

[20] Castanet G, Liénart T, Lemoine F. Dynamics and temperature of droplets impacting onto a heated wall. Int. J. Heat Mass Transf., 2009, 52(3): 670–679. https://doi.org/10.1016/j.ijheatmasstransfer.2008.07.024

[21] Zhao Y, Chen D F, Long M J, et al. Two-dimensional heat transfer model for secondary cooling of continuously cast beam blanks. Ironmak. Steelmak., 2014, 41(5): 377–386. https://doi.org/10.1179/1743281213Y.0000000164

[22] Assuncao C S, Tavares R P, Oliveira G, et al. Comparison of uniform and non-uniform water flux density approaches applied on a mathematical model of heat transfer and solidification for a continuous casting of round billets. Metall. Mater. Trans. B, 2015, 46(1): 366–377. https://doi.org/10.1007/s11663-014-0200-2

[23] Lee P J, Choi H W, Lee S H. The effect of ambient air condition on heat transfer of hot steel plate cooled by an impinging water jet. J. Mech. Sci. Technol., 2003, 17(5): 740–750. https://doi.org/10.1007/BF02983869

[24] Lino R E, Marins A M F, Marchi L A, et al. Influence of the chemical composition on steel casting performance. J. Mater. Res. Technol., 2016, 6(1): 50–56. https://doi.org/10.1016/j.jmrt.2016.05.002

[25] Wang X D, Wang Z F, Liu Y, et al. A particle swarm approach for optimization of secondary cooling process in slab continuous casting. Int. J. Heat Mass Transf., 2016, 93: 250–256. https://doi.org/10.1016/j.ijheatmasstransfer.2015.10.025

[26] Yu Y, Luo X, Zhang H Y, et al. Dynamic optimization method of secondary cooling water quantity in continuous casting based on three-dimensional transient nonlinear convective heat transfer equation. Appl. Therm. Eng., 2019, 160: 113988. https://doi.org/10.1016/j.applthermaleng.2019

[27] Ma J C, Wang B, Zhang D, et al. Optimization of secondary cooling water distribution for improving the billet quality for a small caster. ISIJ Int., 2018, 58(5): 915–920. https://doi.org/10.2355/isijinternational.ISIJINT-2017-711

[28] Ji C, Cai Z Z, Wang W L, et al. Effect of transverse distribution of secondary cooling water on corner cracks in wide thick slab continuous casting process. Ironmak. Steelmak., 2014, 41(5): 360–368. https://doi.org/10.1179/1743281213Y.0000000161

[29] Preuler L, Christian B, Ilie S, et al. Experimental investigations on spray characteristics of water-air nozzles. BHM Berg- und Huttenmannische Monatshefte, 2018, 163(1): 29–36. https://doi.org/10.1007/s00501-017-0693-5

[30] Ramstorfer F, Roland J, Chimani C, et al. Investigation of spray cooling heat transfer for continuous slab casting. Mater. Manuf. Process., 2011, 26(1): 165–168. https://doi.org/10.1080/10426910903206683

[31] Ma H B, Lee J, Tang K, et al. Modeling of spray cooling with a moving steel slab during the continuous casting process. Steel Res. Int., 2019, 90(4): 1800393. https://doi.org/10.1002/srin.201800393

[32] Ma H B, Silaen A, Zhou C. Numerical development of heat transfer coefficient correlation for spray cooling in continuous casting. Front. Mater., 2020, 7: 577265. https://doi.org/10.3389/fmats.2020.577265

[33] Zhang Y Z, Wen Z, Zhao Z W, et al. Velocity characteristics of air-mist jet during secondary cooling of continuous casting using PIV and LDV. ISIJ Int., 2019, 59(6): 1072–1080. https://doi.org/10.2355/isijinternational.ISIJINT-2018-735

[34] Xia Y, Khezzar L, Alshehhi M, et al. Droplet size and velocity characteristics of water-air impinging jet atomizer. Int. J. Multiph. Flow, 2017, 94: 31–43. https://doi.org/10.1016/j.ijmultiphaseflow.2017.04.014

[35] Yan C, Zhang Y, Liu C, et al. Study on the dynamic characteristics of spray droplet in air environment under inclined condition. Nucl. Eng. Des., 2020, 369: 110832. https://doi.org/10.1016/j.nucengdes.2020.110832

[36] Li X, Ouyang J, Wang X, et al. A drag force formula for heterogeneous granular flow systems based on finite average statistical method. Particuology, 2020, 55: 94–107. https://doi.org/j.partic.2020.06.004

[37] Zhou Y. The Research of overspeed atomization behavior in secondary cooling zone of continuous casting. Master Dissertation, Wuhan: Wuhan University of Science and Technology, 2018.

[38] Wei S F, Cheng C G, Zhou Y, et al. Effects of acceleration ring in air passage of continuous casting nozzle on the movement and distribution of liquid phase at nozzle outlet. J. Wuhan Univ. Sci. Technol., 2020, 43(3): 169–175. https://doi.org/10.3969/j.issn.1674-3644.2020.03.002

[39] Tutarova V D, Safonov D S, Shapovalov A N. Density distribution of the spray from flat spray nozzles in the secondary-cooling zone of a continuous caster. Metallurgist, 2012, 56(5–6): 438–442. https://doi.org/10.1007/s11015-012-9594-8

[40] Huerta M E, Mejía M E, Castillejos A H. Heat transfer and observation of droplet-surface interactions during air-mist cooling at CSP secondary system temperatures. Metall. Mater. Trans. B, 2016, 47(2): 1409–1426. https://doi.org/10.1007/s11663-015-0537-1

[41] Martínez-Galván E, Antón, R, Ramos J C, et al. Effect of the spray cone angle in the spray cooling with R134a. Exp. Therm. Fluid Sci., 2013, 50: 127–138. https://doi.org/j.expthermflusci.2013.05.012

[42] Yurishchev A, Ullmann A, Brauner N. Experiments and modeling of droplets motion induced by turbulent air flow on inclined surfaces. Exp. Therm. Fluid Sci., 2023, 140: 110763. https://doi.org/10.1016/j.expthermflusci.2022.110763

[43] D'Urso P, Santoro A. Goodness of fit and variable selection in the fuzzy multiple linear regression. Fuzzy Set. Syst., 2006, 157(19): 2627–2647. https://doi.org/j.fss.2005.03.015

[44] Liu Y J, Wang Q, Li Y G, et al. Prevention of transverse corner cracks in continuously cast steel slabs using asymmetric secondary cooling nozzle. Ironmak. Steelmak., 2011, 38(8): 561–565. https://doi.org/10.1179/1743281211Y.0000000039

[45] Fan H L, Long M J, Yu S, et al. Uniform secondary cooling pattern for minimizing surface reheating of the strand during round bloom continuous casting. JOM, 2018, 70(2): 237–242. https://doi.org/10.1007/s11837-017-2679-x

[46] Wendelstorf J, Spitzer K H, Wendelstorf R. Spray water cooling heat transfer at high temperatures and liquid mass fluxes. Int. J. Heat Mass Transf., 2008, 51(19–20): 4902–4910. https://doi.org/10.1016/j.ijheatmasstransfer.2008.01.032

[47] Zhang J, Chen D F, Zhang C Q, et al. Effects of an even secondary cooling mode on the temperature and stress fields of round billet continuous casting steel. J. Mater. Process. Technol., 2015, 222: 315–326. https://doi.org/10.1016/j.jmatprotec.2015.03.022

[48] Tian Q Y. The research of secondary cooling water distribution technology of thick rectangular billet continuous caster. Master Dissertation, Yanshan: Yanshan University, 2014: 50.

[49] Sheng Y W, Meng X N, Liu X Y. Improved temperature and grain size consistency of continuous cast slabs through cooling spray regulation. Ironmak. Steelmak., 2023, 50(7): 757-765. https://doi.org/10.1080/03019233.2022.2164829